


Configuration mixing in ^{28}Mg and the $^{26}\text{Mg}(t, p)^{28}\text{Mg}$ reaction

D. G. McNeel ^{*}, A. H. Wuosmaa, S. A. Kuvin,[†] and J. Smith


Department of Physics, University of Connecticut, Storrs, Connecticut 06269, USA

B. B. Back , J. Chen, C. R. Hoffman, and B. P. Kay 

Physics Division, Argonne National Laboratory, Argonne, Illinois 60439, USA

G. L. Wilson 

Department of Physics and Astronomy, Louisiana State University, Baton Rouge, Louisiana 70803, USA

D. K. Sharp 

Department of Physics and Astronomy, University of Manchester, Manchester M13 9PL, United Kingdom

R. M. Clark, H. L. Crawford, P. Fallon, and A. O. Macchiavelli

Nuclear Science Division, Lawrence Berkeley National Laboratory, Berkeley, California 94720, USA



(Received 22 January 2021; accepted 18 May 2021; published 16 June 2021)

We have studied the $^{26}\text{Mg}(t, p)^{28}\text{Mg}$ reaction. The nucleus ^{28}Mg lies between ^{24}Mg and ^{32}Mg , the latter of which is central to the “island of inversion” characterized by low-lying neutron fp -shell configurations. The present results show that the second-excited 0^+ state in ^{28}Mg contains large fp -shell occupation for the neutrons. The experiment was performed in inverse kinematics using the HELical Orbit Spectrometer (HELIOS) at Argonne National Laboratory. Shell-model calculations using the SDPF-MU interaction yielded level energies and two-neutron transfer amplitudes that were used in one-step distorted-wave Born approximation calculations to provide theoretical predictions of the proton angular distributions. In many, but not all cases, the data were in good agreement with theoretical predictions.

DOI: [10.1103/PhysRevC.103.064320](https://doi.org/10.1103/PhysRevC.103.064320)

I. INTRODUCTION

The evolution of the shell model for neutron-rich magnesium isotopes has long been an area of interest [1,2]. Studies of binding energies [3,4] and excitation-energy spectra in this region led to the discovery of overbinding and low-lying excited states inconsistent with the expected shell closure at $N = 20$. Experimental results for ^{32}Mg suggested a reordering of shell-model levels [5,6] and strong deformation produced by proton-neutron interactions [1]. This region, commonly referred to as the “island of inversion,” is characterized by nuclides with ground states possessing large fp -shell contributions. This discovery has inspired the development of interactions that highlight the effects of the tensor interaction; these effects are exacerbated by large proton or neutron excess [7–10].

While fp -configuration-dominated ground states characterize nuclei well within the island of inversion, nearby nuclei possess states with similar structure albeit at higher excitation energy. The present work aims to identify states with

similar character in less neutron-rich magnesium nuclei and in particular study the sd - fp shell gap for ^{28}Mg , an isotope of magnesium located midway between stability and the island of inversion.

^{28}Mg is situated exactly between the $N = Z$ nucleus ^{24}Mg and ^{32}Mg ; for the latter, inclusion of the effects due to the proton-neutron imbalance are necessary to explain the structure of low-lying states. In ^{32}Mg , the sd - fp shell gap is small enough that $4p$ - $4h$ neutron configurations must be included to explain the properties of the low-lying 0^+ states [11]. Shell-model calculations using the SDPF-MU [12] interaction may be used to study “intruder” states, in which $2p$ - $2h$ and $4p$ - $4h$ neutron configurations are large.

The two-neutron-adding reaction is well suited to obtain the configuration mixing of final states because it populates those states which closely resemble the ground state of the target nucleus plus two neutrons in single-particle orbits. The theoretical calculation of the corresponding angular distributions is more complicated for two-particle transfer than for single-nucleon transfer. In the (t, p) reaction, the two neutrons are in a relative S state in ^3H , and under the assumption of single-step two-neutron transfer on a spin-zero target, only natural-parity states are populated in the final nucleus.

The $^{26}\text{Mg}(t, p)^{28}\text{Mg}$ reaction has been studied in Refs. [13,14]. These earlier measurements, done in

^{*}dmcneel@lanl.gov; NEN-1, Los Alamos National Laboratory, Los Alamos, NM 87545, USA.

[†]P-27, Los Alamos National Laboratory, Los Alamos, NM 87545, USA.

normal kinematics, used a triton beam at an energy of 3.3 MeV/nucleon. The resulting proton angular distributions were analyzed using a limited plane-wave double stripping theoretical framework. That approach is inadequate for a detailed comparison between theory and experiment as shell-model calculations are necessary to determine the overlaps between the initial and final state of the system needed to make a prediction of the theoretical angular distributions. Furthermore, more than one two-neutron amplitude (TNA) will contribute to the transfer form factor, and these amplitudes can interfere either constructively or destructively. In the present work the energy of the beam was 6.2 MeV/nucleon, and the distorted-wave Born approximation (DWBA) is used in conjunction with shell-model calculations of the TNAs, similar to the procedure described in [15–17].

In this paper we review two-nucleon transfer-reaction theory. We then describe the experiment used to observe the $^{26}\text{Mg}(t, p)^{28}\text{Mg}$ reaction, the data analysis and reduction techniques which were used to produce the excitation-energy spectrum, and the Monte Carlo simulations necessary to produce proton angular distributions. We present the shell-model calculations used to produce the TNAs, and discuss their incorporation into the DWBA formalism to predict the cross sections for different final states. Finally, we compare measured and calculated cross sections, where in many but not all cases the agreement is quite good. Possible reasons for any disagreement will be discussed, and future work will be suggested.

Theory of two-nucleon transfer

The theory of two-nucleon transfer is well documented [15,18,19]. The calculation of the theoretical cross section is separated into a nuclear-structure part, which depends on the nuclear wave functions and the overlap between initial and final states, and the kinematic contributions that accompany the usual DWBA formalism:

$$\frac{d\sigma}{d\Omega} = \sum_M \left| \sum_N G_{NLSJ} B_{NL}^M(\mathbf{k}_1, \mathbf{k}_2) \right|^2. \quad (1)$$

The structure factors G_{NLSJ} [18] contain all information about the internal structure of the initial and final states, where L , S , and J are the orbital, spin, and total angular-momentum transfer, and N identifies different radial wave function. The sum over N is coherent, thus making the DWBA transfer amplitude sensitive to interference between different participating contributions. The factor $B_{NL}^M(\mathbf{k}_1, \mathbf{k}_2)$ incorporates all of the kinematic components of the transfer, and represents the distorted waves in the incoming and outgoing channels. The index M is a summary index for each of the channels with N and L .

In this work, the neutrons of the incoming triton are assumed to be in a relative S state, and are transferred in a single step. This one-step approximation only permits the calculation of cross sections to natural-parity final states. While multistep transfers may contribute, calculation of these processes is outside our treatment.

The structure factors are obtained from shell-model wave functions. For any given final state, the theory produces overlaps between the initial state and each possible configuration in the final state of ^{28}Mg . These are the two-nucleon amplitudes (TNAs). The TNAs play the role of the single-particle form factor for single-nucleon transfer in the DWBA formalism. In contrast to the single-nucleon transfer case, due to the interference between contributing amplitudes, it is impossible to deduce a “spectroscopic factor” for two-nucleon transfer, and instead we can only test for consistency between theoretical predictions and measurement. The nuclear-structure calculations were done using the shell-model code KSHELL as described in Sec. V.

II. EXPERIMENT

The experiment was conducted using HELIOS [20,21] at the ATLAS accelerator at Argonne National Laboratory. The $^{26}\text{Mg}(t, p)^{28}\text{Mg}$ reaction was studied in inverse kinematics with a beam of $^{26}\text{Mg}^{7+}$ at 160.6 MeV (equivalent triton energy 18.6 MeV) and intensity 2×10^7 particles per second incident on a tritiated titanium foil; similar targets have been reported in Ref. [6]. The current target contains between 2.5 and 5.0 $\mu\text{g}/\text{cm}^2$ of tritium. Due to the uncertainty in the amount of tritium contained in the target, we only compare relative normalizations between observed states in ^{28}Mg , which are reported in Sec. V C. Where absolute cross sections are shown, they are estimated from the assumed beam intensity and ^3H content. Deuterated polyethylene (CD_2) $_n$ targets of thicknesses 100 and 240 $\mu\text{g}/\text{cm}^2$ were also used to observe the $^{26}\text{Mg}(d, p)^{27}\text{Mg}$ reaction to provide energy-calibration and transport-efficiency information.

Experimental setup

Reaction products from the $^{26}\text{Mg}(d, p)^{27}\text{Mg}$ and $^{26}\text{Mg}(t, p)^{28}\text{Mg}$ reactions were detected and identified with HELIOS and auxiliary detectors. In HELIOS, a uniform magnetic field produced by a large solenoid aligned with the beam axis causes the charged particles to follow helical trajectories. The protons complete an integral number of orbits before being detected in an array of 24 position-sensitive silicon detectors (PSSDs) along the solenoid axis upstream of the target position. With this arrangement, the proton flight time is a multiple of the cyclotron period T_{cyc} . Here the magnetic field was 2.5 T, and $T_{\text{cyc}} = 26.2$ ns. Center-of-mass quantities such as the residue excitation energy and the scattering angle are deduced from the measured proton energy and distance from the target. The experimental geometry is similar to that used in a number of previous experiments [21–23].

Three different ranges of distance between target and detector were combined to extend the center-of-mass angle coverage of the setup, as listed in Table I. The $^{26}\text{Mg}(d, p)^{27}\text{Mg}$ reaction was measured in all positions, while the $^{26}\text{Mg}(t, p)^{28}\text{Mg}$ reaction was measured in positions $z1$ and $z2$. Depending on the reaction and the geometry of the setup, in many cases it was possible that the protons executed more than one cyclotron orbit. Different numbers of orbits were distinguished using timing measurements as described below.

TABLE I. Array coverage for the three target positions used in the experiment. Angular coverage $\theta_{c.m.}$ is for the ground-state transition in the $^{26}\text{Mg}(t, p)^{28}\text{Mg}$ reaction for positions z_1 and z_2 , including one- and two-orbit protons. These coverages change with excitation energy and number of orbits undergone by the proton. The numbers of proton orbits accepted in the different target positions and reactions are presented under n_{orbits} for the (d, p) and (t, p) reactions.

z_{tgt} (mm)	Array-Target Separation (mm)	Array Coverage (mm)	$\theta_{c.m.}$ (deg)	n_{orbits} (d, p)	n_{orbits} (t, p)
$z_1 = 140$	300	-650 to -300	14° - 50°	1-4	1-2
$z_2 = 340$	500	-850 to -500	31° - 55°	2-7	1-2
$z_3 = -60^a$	100	-450 to -100		1	

^aThis target position was only used for the $^{26}\text{Mg}(d, p)^{27}\text{Mg}$ reaction.

An array of $\Delta E - E$ telescopes of thicknesses $40 \mu\text{m}$ (ΔE detector) and $500 \mu\text{m}$ (E detector) was placed at a fixed position 1042 mm downstream of the geometric center of the solenoid. These detectors subtended a total azimuthal angle of 324° in ϕ and polar angles given in Table I. The geometry of this setup has been simulated in the Monte Carlo simulations described below.

Signals from the silicon-detector arrays were amplified by eight-channel Mesytec preamplifiers. These signals were digitized at a sampling rate of 100 MS/s using a system similar to that used by Digital Gammasphere as described in Refs. [24–26]. Any energy signal from the PSSD array was used as a trigger for the entire system. The digitizer's onboard logic recorded the time stamp for each channel with data, as well as a 2-microsecond-long record of the digitized pulses. These pulse records were used to measure the proton time of flight with sufficient precision to determine the number of cyclotron orbits.

III. DATA REDUCTION AND ANALYSIS

The data were analyzed to eliminate backgrounds from fusion evaporation reactions on the titanium backing foil. Signals from the $\Delta E - E$ detectors were used to select magnesium reaction products, and they provided the time reference for the proton time-of-flight measurements. Essentially all Mg ions have nearly the same velocity, so the time of arrival of the beamlike particles contributes very little to the proton TOF resolution. Finally, the two-body reaction plane was used to establish a correlation between protons detected on each of the PSSD arrays and a specific recoil detector for good events.

Data from the $^{26}\text{Mg}(d, p)^{27}\text{Mg}$ reaction were used to calibrate the detector energy response, and to study the proton-transport efficiency in HELIOS. The separation between target and PSSD array shown in Table I determines the number of allowed proton orbits. For the target separations used in this experiment, up to seven-orbit protons were observed from the $^{26}\text{Mg}(d, p)^{27}\text{Mg}$ reaction and two-orbit protons were observed in the $^{26}\text{Mg}(t, p)^{28}\text{Mg}$ reaction as shown in Table I.

A. Calibration with the $^{26}\text{Mg}(d, p)^{27}\text{Mg}$ reaction

1. Event selection

Three event-selection criteria were developed from the $^{26}\text{Mg}(d, p)^{27}\text{Mg}$ data and were used to separate the $^{26}\text{Mg}(t, p)^{28}\text{Mg}$ reaction products from protons produced by

fusion evaporation. The $\Delta E - E$ telescopes were used to select outgoing magnesium products although the resolution of these detectors was not sufficient to identify different isotopes of magnesium. For the (t, p) measurement, the high rate of particles in the $\Delta E - E$ detectors from elastic scattering off the Ti foil increased the accidental coincidence background. Reaction products were separated from elastic-scattering events as shown in Fig. 1.

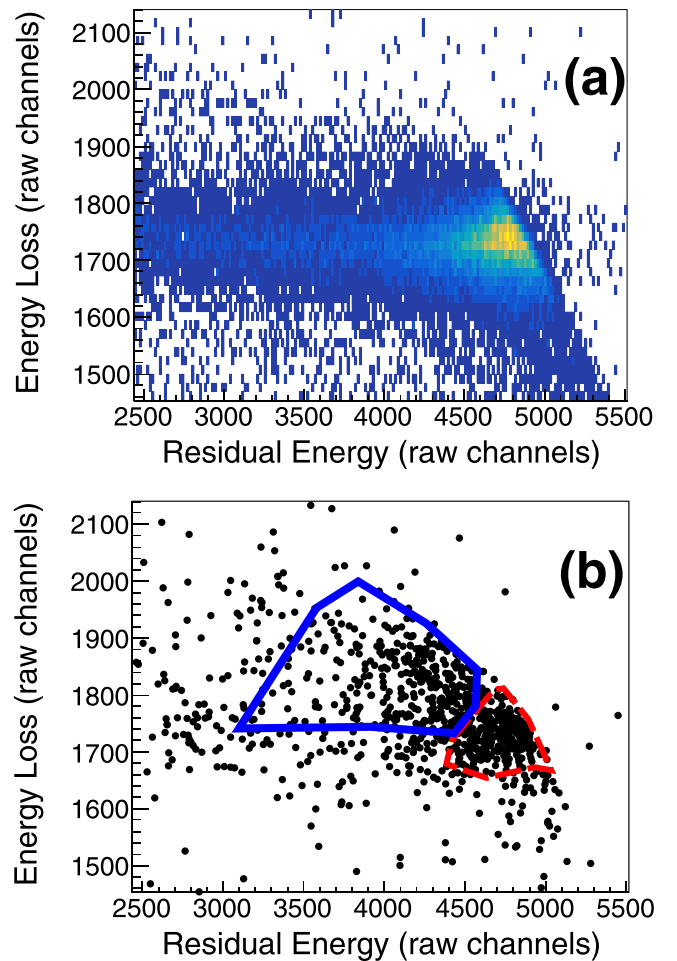


FIG. 1. Recoil-detector particle-identification spectra for the $^{26}\text{Mg}(t, p)^{28}\text{Mg}$ reaction. (a) All detected recoils. (b) Same as (a) for proton- $(\Delta E - E)$ coincidences. The solid blue line indicates the region of interest for reaction products from $^{26}\text{Mg}(t, p)^{28}\text{Mg}$, while the dashed red line indicates the excluded region of elastically scattered ^{26}Mg .

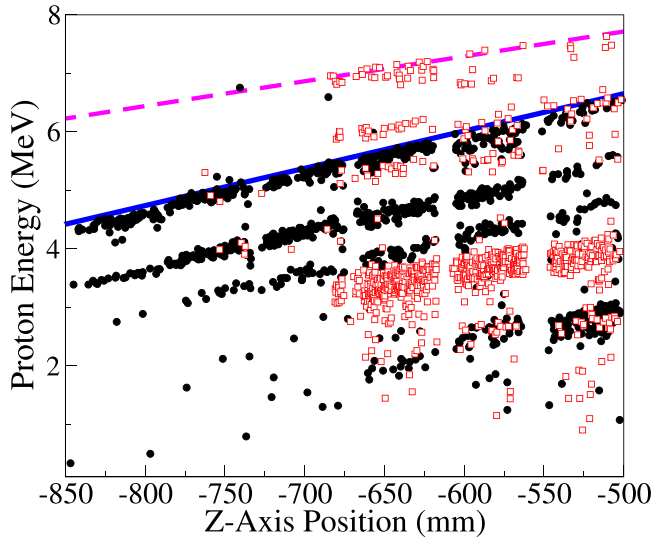


FIG. 2. Proton energy versus position (z) for the $^{26}\text{Mg}(d, p)^{27}\text{Mg}$ reaction. The solid (open) symbols correspond to protons that have executed two (three) cyclotron orbits. The theoretical slopes corresponding to protons from the ground state for two- and three-orbit protons are shown as solid blue and dashed magenta lines, respectively.

2. Digital timing

The number of cyclotron orbits for the protons must be determined. This effect posed a challenge for the analysis, as illustrated in Fig. 2, which shows the relationship between kinetic energy and position for protons from the $^{26}\text{Mg}(d, p)^{27}\text{Mg}$ reaction. The different groups correspond to different excitations in ^{27}Mg ; groups with different slopes correspond to protons with different numbers of cyclotron orbits. Without orbit identification, the different kinematic loci would overlap, complicating the analysis. A digital data timing algorithm was implemented for separating the protons which had undergone more than one orbit. To improve timing, the digital trace data were analyzed to extract a correction based on a polynomial fit to the leading edge of the pulse. This fit is used to determine the start time of the pulse with greater precision than the time stamp, which occurred every 10 ns. The resulting time-of-flight spectrum is shown in Fig. 3 and the resulting timing resolution was 13 ns FWHM, sufficient to resolve the peaks corresponding to a different numbers of orbits.

B. Excitation-energy spectra

The excitation-energy spectra for the $^{26}\text{Mg}(d, p)^{27}\text{Mg}$ reaction for different numbers of proton cyclotron orbits appear in Fig. 4. Figure 5 shows the corresponding spectrum for the $^{26}\text{Mg}(t, p)^{28}\text{Mg}$ reaction for all target positions and proton orbits shown in Table I. The excitation-energy resolutions for the (d, p) and (t, p) measurements were 200 keV and 160 keV (FWHM), respectively.

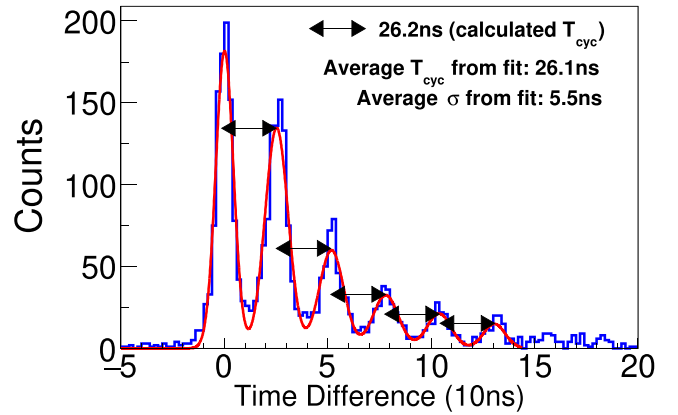


FIG. 3. Time-difference spectrum for the $^{26}\text{Mg}(d, p)^{27}\text{Mg}$ reaction in the z_2 target position. Each peak represents a different number of proton orbits, starting with $n = 2$ (see Table I) and increasing to the right. The peak separation is compared to the expected value of 26.2 ns for six Gaussian peaks.

C. Monte Carlo simulations

We have performed Monte Carlo simulations of the HELIOS setup for the (d, p) and (t, p) reactions. The simulations included the effects of the real magnetic field as measured in Ref. [21], the position and shape of the beam spot, and the shape and position of all detectors and obstacles in the HELIOS volume. The (d, p) data have a very low background and states were visible without recoil coincidence, enabling us to test our Monte Carlo simulations of the recoil coincidence efficiency and to guide the simulations for the $^{26}\text{Mg}(t, p)^{28}\text{Mg}$ reaction. The experimental coincidence efficiency was determined as the ratio of protons observed in singles to those which were subject to all the event selection criteria described in Sec. III A 1. The simulated coincidence efficiency agreed with observation, and has been used to determine the efficiency as a function of measured position along the PSSD

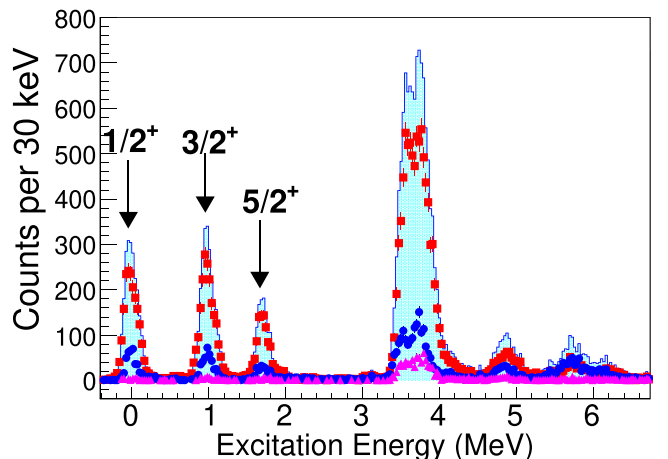


FIG. 4. Excitation-energy spectrum for ^{27}Mg . The spectra shown are excitation energies calculated from the one-, two-, and three-orbit protons (red squares, blue circles, and magenta triangles, respectively) and the sum of all data (histogram).

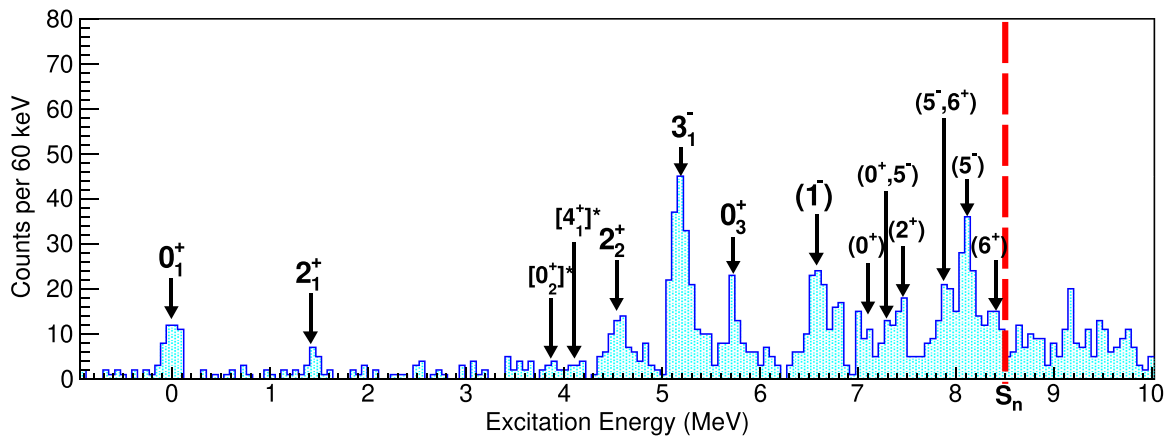


FIG. 5. Excitation-energy spectrum for ^{28}Mg . The asterisk (*) indicates states that are known, but not observed above the level of the background in this work. The position of the 0_2^+ and the 4_1^+ are taken from their literature values. The neutron separation energy is located at the dashed red line, S_n .

array. The $^{26}\text{Mg}(d, p)^{27}\text{Mg}$ data were compared to previous measurements of the angular distributions and found to be in good agreement.

D. Angular distributions

The simulations were used to determine the central center-of-mass angle, and angle range for position bins corresponding to one-half the length of each silicon-array detector. The (d, p) angular distributions were compared to previous data (Ref. [27]) to estimate the incident beam rate. Figure 6 shows the angular distributions of the first three states from the $^{26}\text{Mg}(d, p)^{27}\text{Mg}$ reaction. These angular distributions agree well with those in Ref. [27]. The same analyses were applied to the data from the $^{26}\text{Mg}(t, p)^{28}\text{Mg}$ reaction.

The absolute cross section scale for the (t, p) data has been estimated using the accumulated beam exposure, the estimated amount of ^3H in the target, and systematic uncertainties in the Monte Carlo simulations. These are dominated by our uncertainty in the amount of ^3H in the target which we believe is known at best only to a precision of 30%–40%. All of the results that follow rely on relative cross sections only, and are not subject to any systematic uncertainties in the absolute normalization.

IV. RESULTS

A. Positive-parity states

Angular distributions for the positive-parity states from the $^{26}\text{Mg}(t, p)^{28}\text{Mg}$ reaction are presented in Figs. 7–10. In these figures, the solid red line represents the normalized DWBA calculations described below. Tentative assignments for previously unreported states are based on comparison to DWBA and shell-model predictions of both the shape and relative normalization of the angular distribution as discussed in Sec. V.

1. 0^+ states

The angular distributions for 0^+ states appear in Fig. 7. This figure shows the ground state in panel (a). The data

for the first-excited 0^+ state were not conclusive enough to present an angular distribution because the state was very weakly populated. The second-excited 0^+ state is shown in Fig. 7(b). Here, a possibly unresolved 2^+ state at 5.672 MeV could also be present; however the angular-distribution shape strongly suggests that the peak in this region is dominated by the 0_3^+ excitation. Figure 7(c) shows a possible previously

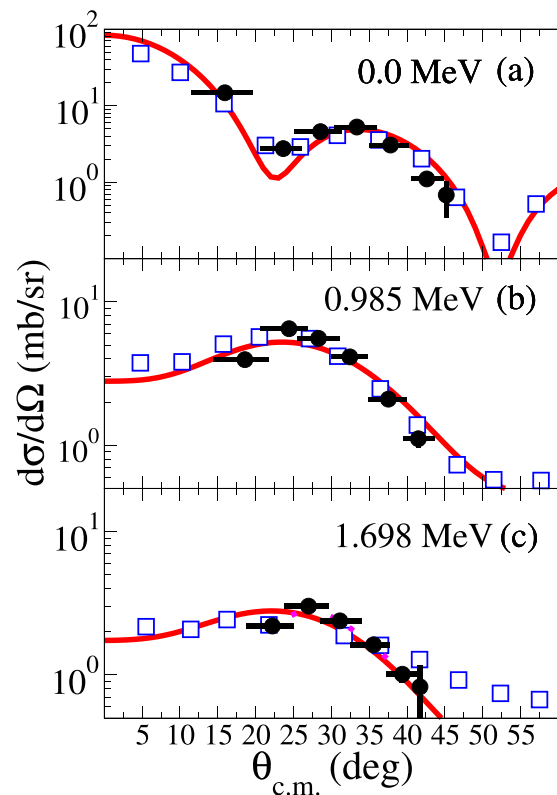


FIG. 6. The first three transitions from the $^{26}\text{Mg}(d, p)^{27}\text{Mg}$ reaction. This experiment (solid black circles) compared to data from Ref. [27] (open blue squares) and DWBA calculations (solid red line).

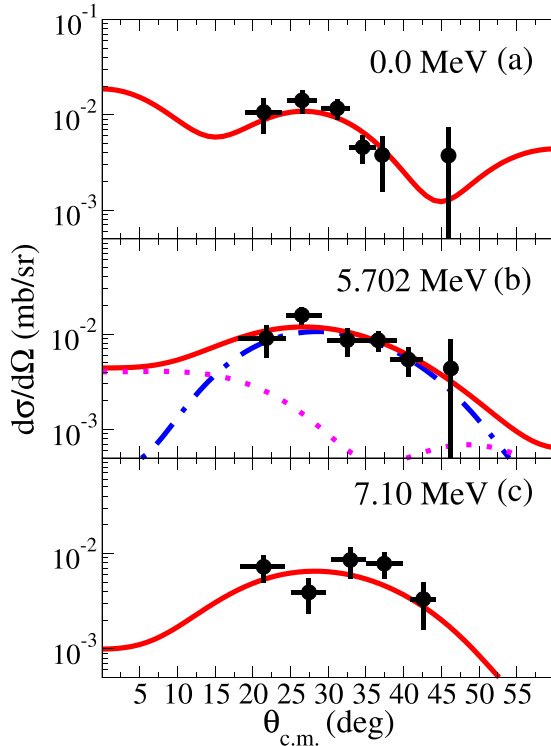


FIG. 7. Proton angular distributions for 0^+ states in ^{28}Mg . Here and for known states the literature values of the excitation energy are displayed. (a) Ground state. (b) 0_3^+ state at 5.702 MeV. In (b), the dot-dashed and dotted curves correspond to the angular distributions calculated for the 0_3^+ and 2^+ (5.672 MeV) excitations. The solid curve in (b) is the sum of these contributions that best reproduces the data. (c) 0^+ state at 7.1 MeV.

unreported state at 7.1 MeV whose angular distribution is most consistent with a 0^+ spin-parity assignment.

The normalization of the ground-state theoretical angular distribution was used as the standard to compare other states with. The strongly populated 0^+ states are the ground state and the 0_3^+ state, and the potential 0^+ state at 7.1 MeV. We note that the angular distributions do not possess the characteristic rise towards 0 degrees often expected for $L = 0$ transitions. This effect can be produced by altering the two-neutron configuration as noted in Ref. [28] or simply changing the bombarding energy. Figure 8 illustrates the bombarding-

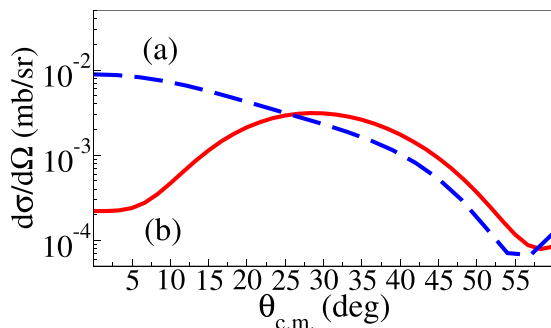


FIG. 8. DWBA angular distributions for the 0_3^+ state at 5.702 MeV calculated at (a) $E(^3\text{H}) = 10$ MeV and (b) $E(^3\text{H}) = 18$ MeV.

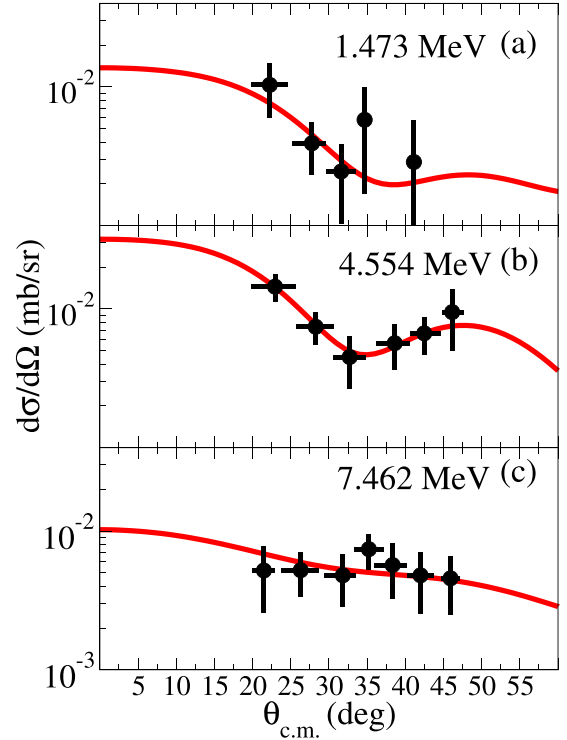


FIG. 9. Angular distribution of protons from observed 2^+ states in ^{28}Mg . The solid curves give the calculated angular distribution with absolute normalization adjusted to best reproduce the data.

energy dependence for this reaction, and shows the calculated DWBA angular distribution at $E(^3\text{H}) = 10$ MeV (used in Ref. [14]) and 18 MeV (current measurement). Both calculations use the same shell-model TNA described below.

2. 2^+ states

Figure 9 shows angular distributions for the well-resolved 2^+ states. The current data are consistent with previous previous assignments for these states. The state shown in Fig. 9(a) (2_1^+) is weakly populated, while those in panels (b) and (c) are more strongly populated. The angular distribution of the 7.4 MeV state shown in Fig. 9(c) is consistent with the tentative assignment of 2^+ (7.462 MeV) [29].

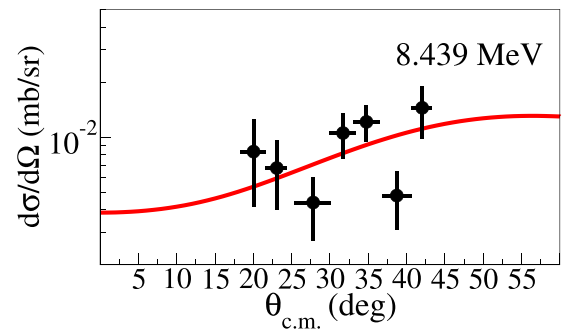


FIG. 10. Angular distribution of protons from the suggested 6^+ state in ^{28}Mg . The solid curve gives the calculated angular distribution with absolute normalization adjusted to best reproduce the data.

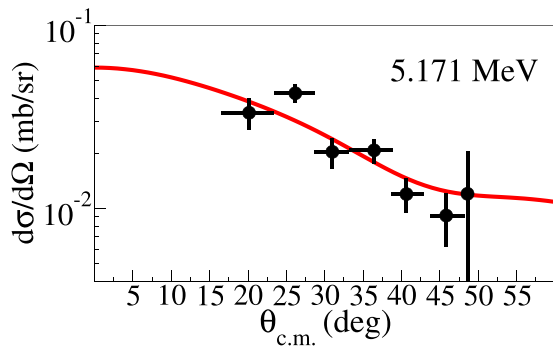


FIG. 11. Angular distribution of protons from observed 3^- state at 5.171 MeV.

3. 6^+ state

Figure 10 shows the angular distribution of a broad state at 8.40 MeV, which may correspond to a 6^+ state suggested in the literature at 8.439 MeV in Ref. [30]. The shape of the angular distribution is consistent with this assignment over the angle range we cover. The lowest 6^+ state calculated in the shell model appears at 8.5 MeV, and is predicted to be weakly populated.

B. Negative-parity states

The negative-parity states provide an estimate of the *sd-fp* shell gap, as they are expected to have simple structures dominated by single-neutron *fp* configurations. Here, we suggest spin-parity assignments based not only on the angular-distribution shape, but also the comparison between the cross section relative to the ground state as predicted by the theory described in Sec. V.

1. 3^- state

Figure 11 shows the angular distribution for the peak at 5.2 MeV. We associate this peak with the 3^- state identified in the compilations at 5.171 MeV based on the angular distribution and the expected strength of the transition resulting from the TNA discussed below. A nearby state with no spin-parity assignment appears at 5.185 MeV in the compilations; Refs. [13,14] suggest a $J^\pi = 1^-$ assignment. If this is correct, then, if it corresponds to the closest 1^- shell-model state, that level is expected to be approximately 6 times weaker than the 3^- , but that contribution would be difficult to disentangle as the 1^- and 3^- angular distributions are quite similar.

2. New negative-parity assignments

Figure 12 shows the angular distributions of several possible negative-parity states. In Fig. 12(a), the solid red line corresponds to a $J^\pi = 1^-$ angular distribution for the peak at 6.60 MeV; several excitations of unknown spin parity are present in this region in the literature, and the shell-model calculation predicts several potential matches. The comparison between theory and experiment discussed below favors a 1^- assignment for this state. In Fig. 12(b), the solid red line is a $J^\pi = 5^-$ angular distribution, while the dash-dotted blue curve is a 0^+ calculation. The angular-distribution shape does

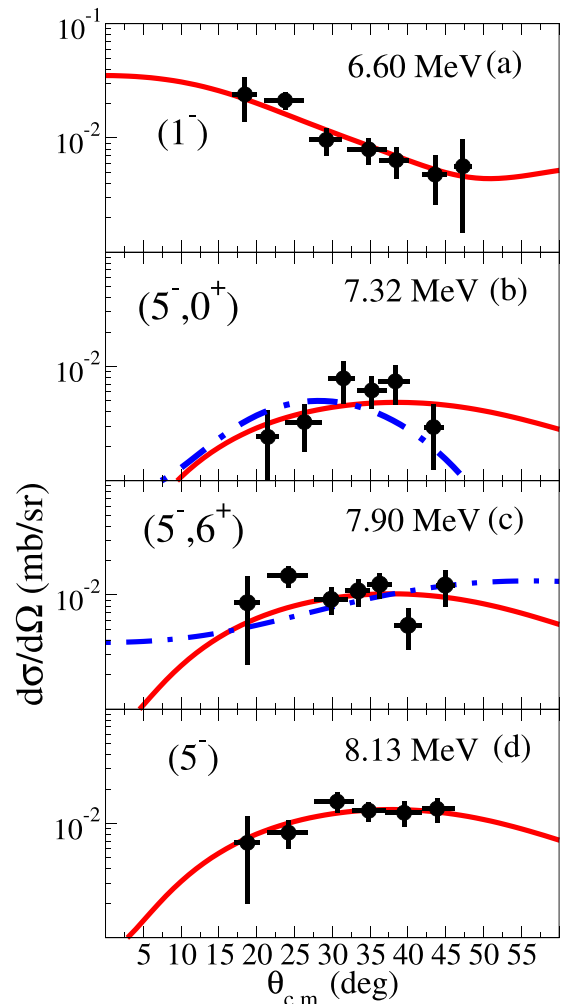


FIG. 12. Angular distribution of protons from potential new negative-parity states. Panel (a) shows the angular distribution for the excitation at 6.60 MeV, with a DWBA 1^- calculation in red. In panel (b), the 5^- angular distribution is the best fit depicted by the solid red line; the dash-dotted blue line is a 0^+ calculation. In panel (c) dash-dotted blue line is a 6^+ calculation. Finally, panel (d) displays data from a newly observed state at 8.13 MeV. For all states, the normalization prefers the 5^- assignment.

not strongly distinguish between these values, although there is a slight preference from the normalization factor discussed below for a 5^- assignment. For the state at 7.9 MeV in Fig. 12(c) the solid red curve is again a 5^- calculation, while the dash-dotted blue curve is a 6^+ calculation. Here again the shapes do not discriminate between these two choices, although the normalization between theory and experiment strongly favors the 5^- assignment. Finally, a newly observed state at 8.1 MeV has been tentatively assigned $J^\pi = 5^-$ spin and parity.

V. THEORETICAL ANALYSIS

We have used shell-model calculations to help understand the properties of states in ^{28}Mg , and to help interpret the results of our $^{26}\text{Mg}(t, p)^{28}\text{Mg}$ measurement. In addition to a

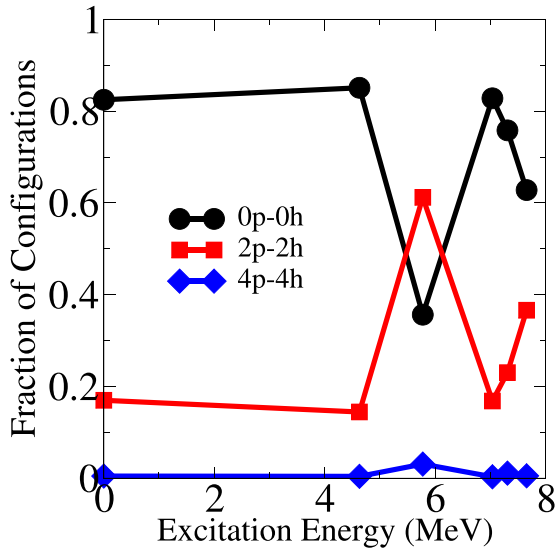


FIG. 13. Particle-hole content for the first six 0^+ states. The second-excited 0^+ state is dominated by 2p-2h configurations. The 4p-4h content is almost negligible for ^{28}Mg , with a maximum of 3% in the intruder state.

predicted level scheme, we have also used the shell model to compute the TNAs that are necessary for DWBA calculations of the proton angular distributions. The calculated DWBA angular distributions can then be compared to the experimental data to establish consistency between theory and experiment, and to support spin-parity assignments for possible new states in ^{28}Mg .

A. Shell-model calculations

We have performed shell-model calculations in the sd - fp model space using the shell-model code KHELL [31]. For all calculations, we have used the SDPF-MU interaction [9]. To make the calculations tractable with the computer resources available, the valence-nucleon space was truncated, confining all valence protons to the sd shell, and permitting no more than four neutrons to be promoted to the fp shell.

The calculations yielded excitation energies, orbital occupancies, and the amplitudes of different two-neutron sd - pf configurations for states in ^{28}Mg . The proton and neutron occupation numbers in ^{28}Mg are presented in Table IV of the Appendix. The TNAs were then used to calculate the theoretical angular distributions as discussed below. The wave functions from the shell-model calculation were analyzed to identify cross-shell excitations in ^{28}Mg .

The predicted excitation energies, spins, and parities for states in ^{28}Mg are listed in Table II. In many cases, experimental counterparts for the predicted excitations are not yet identified. Below 6 MeV, the agreement between theory and experiment is quite reasonable.

The 0^+ states are particularly interesting, as they most cleanly reveal the presence of the lowest cross-shell excitations and can be strongly populated in two-neutron transfer reactions. Figure 13 shows the strengths of neutron-particle-hole pair excitations for the six lowest calculated 0^+ states.

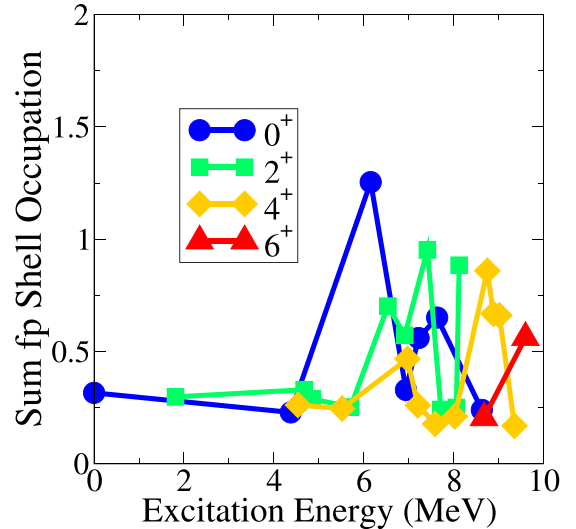


FIG. 14. Total fp -shell occupation from the shell model calculations as a function of excitation energy for the positive-parity states.

These results reveal, as expected, that the ground state is dominated by neutron 0p-0h configurations, with a 17% neutron 2p-2h component. The 0_3^+ state is identified as an intruder configuration with predominantly neutron 2p-2h nature as illustrated in Fig. 13. This state contains 61% 2p-2h configurations and 36% 0p-0h content, and is the only 0^+ state below 10 MeV excitation energy with any non-negligible 4p-4h content (approximately 4%). This transition to large fp content signals the opening of the fp shell to other states. As seen in Fig. 14, once the excitation energy passes 6 MeV fp -shell occupation becomes more pronounced for the positive-parity states. Also, the negative-parity states which must be single- fp neutron excitations only appear above the 0_3^+ state in the calculations, although the first of these in the experimental spectrum, the 3_1^- level, is below the experimental 0_3^+ excitation.

B. DWBA calculations

The angular-distribution calculations were performed using the zero-range DWBA code DWUCK4 [32]. For the purposes of the current investigation, finite-range effects have a small influence on the shape and magnitude of the angular distribution. Finite range corrections were also investigated for the current reaction and found to be negligible over the angle ranges covered for this experiment. The optical-model potential parameters for the calculation were taken from global optical-model potential sets for the triton [33] (incoming channel) and proton [34] (outgoing channel). These values are given in Table III for the ground state to ground state transitions. Some of the optical-model parameters depend slightly on excitation energy as described in Refs. [33,34]. The form factors used in the DWBA transition amplitude were calculated using the TNAs obtained from the shell-model calculations described above. This procedure is described in detail below.

TABLE II. Excitation energies, spins, and parities of states below 8.5 MeV in ^{28}Mg from the present measurement and from the literature (from [29] unless otherwise noted).

^{28}Mg					
Present Experiment		Literature		Shell-Model Calculation	
E_X (MeV)	J^π	E_X (MeV)	J^π	E_X (MeV)	J^π
0	0^+	0	0^+	0	0_1^+
1.46	2^+	1.474	2^+	1.859	2_1^+
		3.862	0^+	4.631	0_2^+
		4.021	4^+	4.643	4_1^+
4.58	2^+	4.555	2^+	4.784	2_2^+
		4.561	1^+	5.015	2_3^+
4.87		4.879	2^+	5.478	1_1^+
5.20	3^-	5.171	3^-	5.661	4_2^+
		5.185		5.778	0_3^+
		5.193	1	5.858	2_4^+
		5.270	1^+	5.922	3_1^+
5.41		5.47	2	6.316	2_1^-
		5.672	2^+	6.334	3_1^-
5.75	0^+	5.702	0^+	6.422	1_2^+
5.95		5.917	$(0, 1, 2)^+$	6.450	1_1^-
6.11		6.135 ^a	$(0, 4)^-$	6.498	2_5^+
6.39		6.416		6.638	4_1^-
		6.516		6.893	3_2^+
		6.544	(2^+)	6.933	2_6^+
6.60	(1^-)	6.599		6.975	4_3^+
		6.708		7.039	0_4^+
6.80		6.759		7.206	4_4^+
7.10	(0^+)			7.250	1_3^+
		7.201	$(0, 1, 2)^+$	7.268	1_2^-
7.32	$(5^-, 0^+)$			7.275	3_3^+
7.46	(2^+)	7.462	(2^+)	7.311	0_5^+
7.90	$(5^-, 6^+)$	7.929	(6^+)	7.356	3_4^+
8.13	(5^-)			7.409	2_7^+
8.44	(6^+)	8.439 ^a	(6^+)	7.513	5_1^-
				7.585	3_2^-
				7.591	4_5^+
				7.598	0_1^-
				7.658	0_6^+
				7.720	2_8^+
				7.733	4_2^-
				7.806	3_5^+
				8.018	5_2^-
				8.028	4_6^+
				8.057	2_2^-
				8.063	2_9^+
				8.109	3_3^-
				8.120	1_4^+
				8.125	2_{10}^+
				8.156	3_6^+
				8.257	1_5^+
				8.416	2_3^-

^aThis level was reported in Ref. [30].

TNAs and the form factor

The form factors in the DWBA amplitude are obtained from a coherent sum over the individual two-nucleon form factors for each configuration, with magnitudes and phases

taken from the shell-model calculations. We follow the usual prescription Refs. [15–17] that the form factors are obtained using a Woods-Saxon well for each neutron, where the depth is adjusted to fit the binding energy of each neutron which

TABLE III. Table of global optical model parameters used in this work. V , r_0 , a , and W correspond to the real well depth, radius parameter, diffuseness parameters, and imaginary well depth. The real- and imaginary-volume potentials do not have subscripts, while s indicates the imaginary-surface potential and so the real and imaginary spin-orbit potentials. r_C is the usual Coulomb radius parameter. The well depth varies slightly with energy, so parameters are calculated for each state in the outgoing channel (protons). The parameters for the ground state to ground state transitions are presented.

Channel	V	r_0	a	W	r_0	a	W_s	r_{0s}	a_s	V_{so}	r_{0so}	a_{so}	W_{so}	r_{0so}	a_{so}	r_C
$^{26}\text{Mg}+d$	81.81	1.174	0.80				16.64	1.328	0.59	3.70	1.234	0.81	-0.21	1.23	0.81	1.70
$^{26}\text{Mg}+t$	116.6	1.14	0.82	2.36	1.27	0.84	17.52	1.27	0.84	1.33	1.04	0.13				1.28
$^{27}\text{Mg}+p$	52.83	1.17	0.67	1.43	1.17	0.67	8.53	1.30	0.53	5.44	0.97	0.59	-0.07	0.97	0.59	1.33
$^{28}\text{Mg}+p$	50.05	1.17	0.67	2.40	1.17	0.67	7.93	1.29	0.53	5.26	0.97	0.59	-0.13	0.97	0.59	1.32
$^{26}\text{Mg}+n$		1.28	0.65								1.1	0.65				1.3
$^{26}\text{Mg}+2n$		1.28	0.65							25						1.3

is fixed at one-half the experimental two-neutron binding energy.

As an example, the total form factors for the three lowest 0^+ states appear in Fig. 15. The total form factor for 0^+ states in our shell model space contains seven possible configurations: $(0d_{5/2}^2)^2$, $(0d_{3/2}^2)^2$, $(1s_{1/2}^2)^2$, $(0f_{7/2}^2)^2$, $(0f_{5/2}^2)^2$, $(1p_{3/2}^2)^2$, and $(1p_{1/2}^2)^2$. The relative weakness of the 0_2^+ state compared to the ground state can be traced to the small form factor near the nuclear surface as seen in Fig. 15(b). The shape of the 0_3^+ form factor, with its additional node, is characteristic of an $(fp)^2$ -dominated excitation, and it too is large near the nuclear surface.

The form factor for the 3^- state is shown in Fig. 15(d) for comparison. As expected, it is also larger near the nuclear surface. This strength, combined with favorable angular momentum matching conditions for $L = 3$ transfer, make this the most strongly populated state in the reaction.

C. Comparison to experiment and discussion

The experimental angular distributions were compared to the theoretical results. The normalization between theory and experiment for each excited state was compared to the ground state to remove systematic uncertainty associated with absolute the normalization. The normalization between theory and experiment is given by

$$\frac{d\sigma}{d\Omega_{\text{exp}}} = f_i f_g \frac{d\sigma}{d\Omega_{\text{theory}}}, \quad (2)$$

where f_g is the normalization factor for the ground state and f_i is an additional factor for each excited state. The normalization factors f_i are shown in Fig. 16; they were obtained by dividing the normalization factor by the ground-state normalization factor $f_g = 2.92 \pm 0.43$.

The normalization factors were used as one criterion for matching an observed excitation to a shell-model state. For example, the state at 6.6 MeV was determined to match an angular distribution with $J^\pi = 1^-$. The shell-model calculations indicated that the 1_1^- state is nearly degenerate with the 3_1^- state, which may be experimentally corroborated by the presence of a $J = 1$ state of undetermined parity at 5.193 MeV in the literature; however the experimental resolution was not sufficient to resolve this state. The DWBA calculation for the 1_1^- state showed that the state is expected to be weakly

populated; however, the 1_2^- state was predicted to be strongly populated. Using the DWBA calculation for the 1_2^- angular distribution, the 6.6 MeV state had a normalization factor

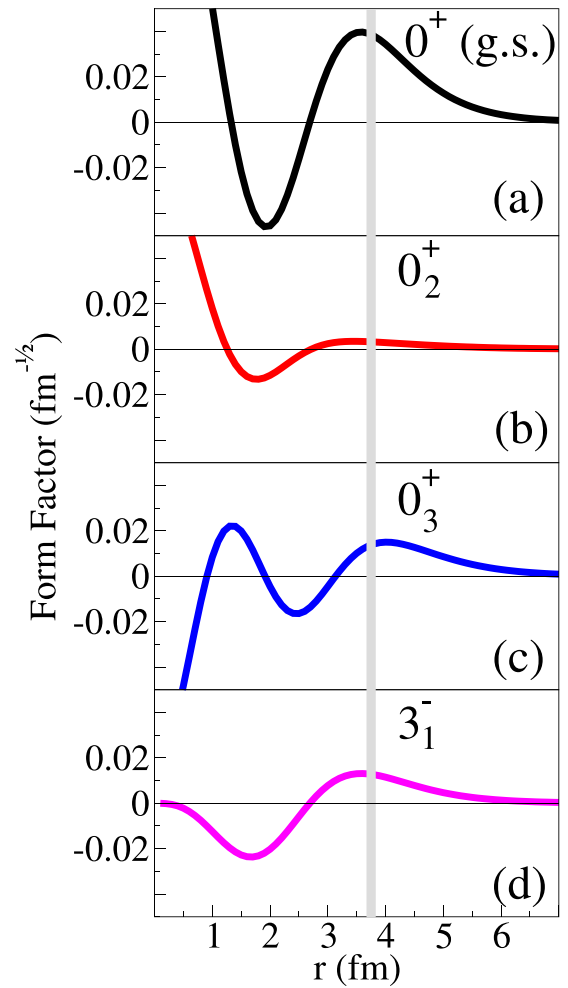


FIG. 15. Form factors for the first three 0^+ states and the first 3^- state. The ground state (a) and second-excited 0^+ state (c) have some amplitude at the nuclear surface, while the first-excited state (b) is small. The form factor for the 3^- state is also shown in panel (d). The gray bar indicates the approximate location of the nuclear surface.

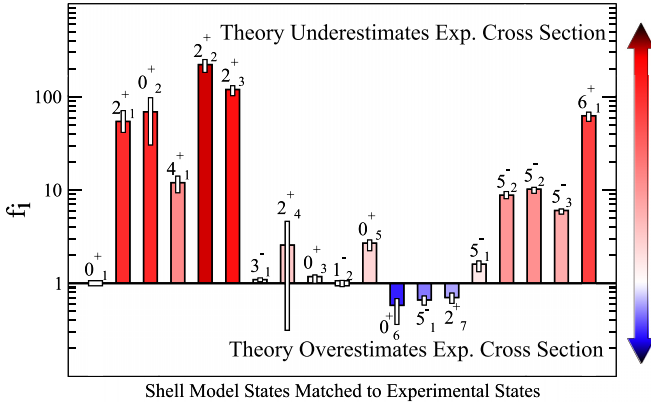


FIG. 16. The individual normalization factors f_i after the global normalization factor has been removed. The statistical uncertainty of the value is indicated by the length of the white rectangular box. States with a normalization factor greater than 1 have cross sections that are underestimated by theory, while a normalization less than 1 indicates an overestimation by theory.

of 2.90 ± 0.32 . Since this is equivalent to the ground-state normalization factor, and there was excellent agreement with the calculated angular distribution, it was determined that the shell-model 1_2^- state best describes the observed 6.6 MeV excitation.

Figure 16 shows that the most strongly populated states are better described by theory. These include the 3_1^- , the 0_3^+ , and the 1_2^- . When the predicted cross section is small, the agreement between theory and experiment is poor, and the relative normalization factor is large. For example, the cross section of the 2^+ excitation is not well described by the theory, which underestimates the cross section by a factor of

more than 100. Possible explanations for such disagreements for this or other weakly populated states include background contributions to the yield, or other second-order processes that are not considered in the reaction calculation. Finally, as excitation energy increases, the increased level density makes it more difficult to associate observed peaks with calculated levels.

VI. SUMMARY AND CONCLUSIONS

We have studied the $^{26}\text{Mg}(t, p)^{28}\text{Mg}$ reaction to obtain information about sd - fp cross-shell excitations between the valley of stability and the island of inversion. A comparison between theory and experiment of the angular distributions and relative normalizations helped confirm existing spin assignments, and suggested new tentative assignments for a number of previously unassigned excitations. Shell-model calculations with the SDPF-MU interaction, which incorporates the tensor interaction and has been applied to nuclei in the region of the island of inversion, have been used to confirm cross-shell fp -dominated states in ^{28}Mg that are strongly populated in the $^{26}\text{Mg}(t, p)^{28}\text{Mg}$ reaction.

The population strength and the angular distribution of protons from the $^{26}\text{Mg}(t, p)^{28}\text{Mg}$ reaction were calculated using the coherent addition of the TNAs calculated in the shell model. Some observed states were not in agreement with the cross section predicted by the theoretical analysis of this work; one possible reason for this disagreement is that two-step processes are not included in the analysis. For a number of states at higher excitation energies, it becomes more difficult to match the shell-model states to the observed excitations; when this has been done in this work, we have used the prediction of the total cross section, the predicted

TABLE IV. Shell-model occupation numbers for the selected states in $^{26,28}\text{Mg}$ calculated with the SDPF-MU interaction. Only those states shown in Fig. 16 are presented. Positive-parity states with a total neutron fp -shell occupation greater than 0.5 are in bold.

Nucleus	E_x (MeV)	J_n^π	Protons			Neutrons						
			$0d_{5/2}$	$0d_{3/2}$	$1s_{1/2}$	$0d_{5/2}$	$0d_{3/2}$	$1s_{1/2}$	$0f_{7/2}$	$0f_{5/2}$	$1p_{3/2}$	$1p_{1/2}$
^{26}Mg	0.000	0_1^+	3.129	0.529	0.342	4.520	0.743	0.600	0.082	0.031	0.016	0.007
^{28}Mg	0	0_1^+	3.317	0.38	0.303	5.273	1.272	1.095	0.228	0.057	0.058	0.018
	1.859	2_1^+	3.309	0.336	0.355	5.278	1.353	1.028	0.212	0.054	0.058	0.017
	4.631	0_2^+	3.326	0.426	0.247	5.455	1.032	1.214	0.194	0.040	0.054	0.010
	4.643	4_1^+	3.395	0.275	0.330	5.261	1.278	1.166	0.180	0.050	0.049	0.015
	4.784	2_2^+	3.173	0.364	0.463	4.961	1.383	1.245	0.266	0.052	0.077	0.017
	5.015	2_3^+	3.324	0.400	0.276	5.039	1.364	1.310	0.177	0.044	0.052	0.014
	5.778	0_3^+	2.937	0.566	0.497	4.637	1.092	0.922	0.804	0.078	0.414	0.053
	5.858	2_4^+	2.915	0.422	0.663	5.166	1.179	1.357	0.177	0.047	0.057	0.017
	6.334	3_1^-	3.092	0.522	0.386	5.256	0.868	0.815	0.701	0.057	0.282	0.022
	7.268	1_2^-	3.075	0.494	0.432	5.010	0.884	1.031	0.217	0.061	0.575	0.222
	7.311	0_5^+	3.296	0.374	0.330	5.126	1.465	0.902	0.259	0.049	0.172	0.027
	7.409	2_7^+	3.178	0.458	0.365	5.051	1.282	1.032	0.360	0.050	0.193	0.032
	7.513	5_1^-	3.123	0.493	0.383	5.198	1.132	0.601	0.827	0.063	0.164	0.015
	7.658	0_6^+	3.030	0.429	0.540	4.387	1.461	1.398	0.485	0.056	0.184	0.030
	8.018	5_2^-	3.019	0.501	0.480	4.652	1.100	1.133	0.825	0.051	0.228	0.012
	8.734	6_1^+	3.423	0.298	0.279	5.140	1.513	1.111	0.140	0.042	0.043	0.012
	9.395	5_3^-	2.959	0.559	0.482	4.853	0.986	1.088	0.802	0.061	0.196	0.013

energy, and the shape of the angular distribution to attempt a spin-parity assignment.

The angular distributions and observed cross section were found to be in good agreement with theoretical predictions for the intruder 0_3^+ state and strongly populated states which were the primary motivation for the experiment. Future measurements that sample more forward angles would also be useful to better characterize the angular distributions for transitions to 0^+ states. This shows that the SDPF-MU interaction is widely applicable to nuclei in the *sd-fp* region.

In future work on the magnesium isotopes, these experimental methods could be used to track the evolution of the *fp*-shell gap for isotopes approaching ^{32}Mg . The appearance of intruder states at lower excitation energies can be confirmed by two-neutron adding, because these states are well described by one-step transfer of two neutrons into the *fp* shell. Another interesting avenue for calculation is the evolution of the intruder state with changing proton number, for example, the isotopes from ^{40}Ca to ^{32}Mg . A recent paper by Miyagi *et al.* [35] studied the evolution of the cross-shell *fp*-dominated states in the magnesium isotopes. Those calculations are in qualitative agreement with our work, although Ref. [35] does not discuss the 0_3^+ state in ^{28}Mg which is dominated by *fp*

configurations. This work shows that detailed spectroscopy of (*t*, *p*) reactions is a valuable tool for tracking the evolution of this type of state with respect to increasing neutron number.

ACKNOWLEDGMENTS

This material is based on work supported by the US Department of Energy, Office of Science, Office of Nuclear Physics, under Awards No. DE-SC0014552 and No. DE-AC02-06CH11357, and the US National Science Foundation under Grant No. PHY-1068217. D.K.S. was supported by the UK Science and Technology Facilities Council (Grant No. ST/P004423/1). This research used resources of the Argonne National Laboratory ATLAS Accelerator Facility, which is a Department of Energy Office of Science User Facility. The authors also thank Prof. N. Shimizu for helpful discussions regarding the shell-model calculations.

APPENDIX: TABLE OF OCCUPATION NUMBERS

The occupation numbers from the shell-model calculation described in Sec. V A are presented in Table IV.

-
- [1] B. H. Wildenthal and W. Chung, *Phys. Rev. C* **22**, 2260 (1980).
 [2] E. K. Warburton, J. A. Becker, and B. A. Brown, *Phys. Rev. C* **41**, 1147 (1990).
 [3] C. Thibault, R. Klapisch, C. Rigaud, A. M. Poskanzer, R. Prieels, L. Lessard, and W. Reisdorf, *Phys. Rev. C* **12**, 644 (1975).
 [4] C. Détraz, M. Langevin, D. Guillemaud, M. Epherre, G. Audi, C. Thibault, and F. Touchard, *Nucl. Phys. A* **394**, 378 (1983).
 [5] M. H. Storm, A. Watt, and R. R. Whitehead, *J. Phys. G* **9**, L165 (1983).
 [6] K. Wimmer, T. Kröll, R. Krücken, V. Bildstein, R. Gernhäuser, B. Bastin, N. Bree, J. Diriken, P. Van Duppen, M. Huysse, N. Patronis, P. Vermaelen, D. Voulot, J. Van de Walle, F. Wenander, L. M. Fraile, R. Chapman, B. Hadinia, R. Orlandi, J. F. Smith *et al.*, *Phys. Rev. Lett.* **105**, 252501 (2010).
 [7] T. Otsuka, R. Fujimoto, Y. Utsuno, B. A. Brown, M. Honma, and T. Mizusaki, *Phys. Rev. Lett.* **87**, 082502 (2001).
 [8] T. Otsuka, T. Suzuki, R. Fujimoto, H. Grawe, and Y. Akaishi, *Phys. Rev. Lett.* **95**, 232502 (2005).
 [9] T. Otsuka, *Phys. Scr.* **T152**, 014007 (2013).
 [10] T. Otsuka and Y. Tsunoda, *J. Phys. G: Nucl. Part. Phys.* **43**, 024009 (2016).
 [11] A. O. Macchiavelli, H. L. Crawford, C. M. Campbell, R. M. Clark, M. Cromaz, P. Fallon, M. D. Jones, I. Y. Lee, M. Salathe, B. A. Brown, and A. Poves, *Phys. Rev. C* **94**, 051303(R) (2016).
 [12] Y. Utsuno, T. Otsuka, B. A. Brown, M. Honma, T. Mizusaki, and N. Shimizu, *Phys. Rev. C* **86**, 051301(R) (2012).
 [13] S. Hinds, H. Marchant, and R. Middleton, *Proc. Phys. Soc.* **78**, 473 (1961).
 [14] R. Middleton and D. J. Pullen, *Nucl. Phys.* **51**, 77 (1964).
 [15] P. W. Keaton, D. D. Armstrong, L. R. Veaser, H. T. Fortune, and N. R. Roberson, *Nucl. Phys. A* **179**, 561 (1972).
 [16] R. H. Ibarra, M. Vallieres, and D. H. Feng, *Nucl. Phys. A* **241**, 386 (1975).
 [17] H. T. Fortune, M. E. Cobern, S. Mordechai, G. E. Moore, S. LaFrance, and R. Middleton, *Phys. Rev. Lett.* **40**, 1236 (1978).
 [18] N. K. Glendenning, *Phys. Rev.* **137**, B102 (1965).
 [19] B. F. Bayman, *Nucl. Phys. A* **168**, 1 (1971).
 [20] A. H. Wuosmaa, J. P. Schiffer, B. B. Back, C. J. Lister, and K. E. Rehm, *Nucl. Instrum. Methods Phys. Res., Sect. A* **580**, 1290 (2007).
 [21] J. C. Lighthall, B. B. Back, S. I. Baker, S. J. Freeman, H. Y. Lee, B. P. Kay, S. T. Marley, K. E. Rehm, J. E. Rohrer, J. P. Schiffer, D. V. Shetty, A. W. Vann, J. R. Winkelbauer, and A. H. Wuosmaa, *Nucl. Instrum. Methods A* **622**, 97 (2010).
 [22] C. R. Hoffman, B. B. Back, B. P. Kay, J. P. Schiffer, M. Alcorta, S. I. Baker, S. Bedoor, P. F. Bertone, J. A. Clark, C. M. Deibel, B. DiGiovine, S. J. Freeman, J. P. Greene, J. C. Lighthall, S. T. Marley, R. C. Pardo, K. E. Rehm, A. Rojas, D. Santiago-Gonzalez, D. K. Sharp *et al.*, *Phys. Rev. C* **85**, 054318 (2012).
 [23] J. Chen, C. R. Hoffman, T. Ahn, K. Auranen, M. L. Avila, B. B. Back, D. W. Bardayan, D. Blankstein, P. Copp, D. Gorelov, B. P. Kay, S. A. Kuvin, J. P. Lai, D. G. McNeel, P. D. O'Malley, A. M. Rogers, D. Santiago-Gonzalez, J. P. Schiffer, J. Sethi, R. Talwar *et al.*, *Phys. Rev. C* **98**, 014325 (2018).
 [24] M. Cromaz, V. J. Riot, P. Fallon, S. Gros, B. Holmes, I. Y. Lee, A. O. Macchiavelli, C. Vu, H. Yaver, and S. Zimmermann, *Nucl. Instrum. Methods Phys. Res., Sect. A* **597**, 233 (2008).
 [25] S. Zimmermann, J. T. Anderson, D. Doering, J. Joseph, C. Lionberger, T. Stezelberger, and H. Yaver, in *2011 IEEE Nuclear Science Symposium Conference Record, Valencia, Spain* (IEEE, Piscataway, NJ, 2011), pp. 596–601.
 [26] J. T. Anderson, M. Albers, M. Alcorta, C. Campbell, M. P. Carpenter, C. J. Chiara, M. Cromaz, H. M. David, D. Doering,

- D. T. Doherty, C. R. Hoffman, R. V. F. Janssens, J. Joseph, T. L. Khoo, A. Kreps, T. Lauritsen, I. Y. Lee, C. Lionberger, C. J. Lister, T. Madden *et al.*, in *2012 IEEE Nuclear Science Symposium and Medical Imaging Conference Record (NSS/MIC)*, Anaheim, California (IEEE, Piscataway, NJ, 2012), pp. 1536–1540.
- [27] F. Meurders and A. V. D. Steld, *Nucl. Phys. A* **230**, 317 (1974).
- [28] H. T. Fortune, R. Middleton, M. E. Cobern, G. E. Moore, S. Mordechai, R. V. Kollarits, H. Nann, W. Chung, and B. H. Wildenthal, *Phys. Lett. B* **70**, 408 (1977).
- [29] M. S. Basunia, *Nucl. Data Sheets* **114**, 1189 (2013).
- [30] J. Williams, G. C. Ball, A. Chester, T. Domingo, A. B. Garnsworthy, G. Hackman, J. Henderson, R. Henderson, R. Krücken, A. Kumar, K. D. Launey, J. Measures, O. Paetkau, J. Park, G. H. Sargsyan, J. Smallcombe, P. C. Srivastava, K. Starosta, C. E. Svensson, K. Whitmore *et al.*, *Phys. Rev. C* **100**, 014322 (2019).
- [31] N. Shimizu, T. Mizusaki, Y. Utsuno, and Y. Tsunoda, *Comput. Phys. Commun.* **244**, 372 (2019).
- [32] P. D. Kunz and E. Rost, The distorted-wave born approximation, in *Computational Nuclear Physics 2: Nuclear Reactions*, edited by K. Langanke, J. A. Maruhn, and S. E. Koonin (Springer, New York, 1993), pp. 88–107.
- [33] D. Y. Pang, P. Roussel-Chomaz, H. Savajols, R. L. Varner, and R. Wolski, *Phys. Rev. C* **79**, 024615 (2009).
- [34] A. Koning and J. Delaroche, *Nucl. Phys. A* **713**, 231 (2003).
- [35] T. Miyagi, S. R. Stroberg, J. D. Holt, and N. Shimizu, *Phys. Rev. C* **102**, 034320 (2020).